Draft of November 10, 2020
Preprint typeset using LaTeX style emulateapj v. 12/16/11

arXiv:1808.04232v2 [astro-ph.HE] 7 Nov 2020

SUPERNOVA PTF 12GLZ: A POSSIBLE SHOCK BREAKOUT DRIVEN THROUGH AN ASPHERICAL WIND

Maayane T. Soumagnac[1], Eran O. Ofek[1], Avishay Gal-yam[1], Eli Waxman [1], Sivan Ginzburg [2], Nora Linn Strotjohann[3], Tom A. Barlow[4], Ehud Behar[5], Doron Chelouche[6], Christoffer Fremling [7], Noam Ganot [1], Suvi Gezari[8], Mansi M. Kasliwal [9], Shai Kaspi[12], Shrinivas R. Kulkarni [9], Russ R. Laher[11], Dan Maoz[12], Christopher D. Martin[4], Ehud Nakar[12], James D. Neill[4], Peter E. Nugent [13,14], Dovi Poznanski[12], Steve Schulze[1], Ofer Yaron[1]

Draft of November 10, 2020

ABSTRACT

We present visible-light and ultraviolet (UV) observations of the supernova PTF 12glz. The SN was discovered and monitored in near-UV and R bands as part of a joint *GALEX* and Palomar Transient Factory campaign. It is among the most energetic Type IIn supernovae observed to date ($\approx 10^{51}$ erg). If the radiated energy mainly came from the thermalization of the shock kinetic energy, we show that PTF 12glz was surrounded by $\sim 1\,M_\odot$ of circumstellar material (CSM) prior to its explosive death. PTF 12glz shows a puzzling peculiarity: at early times, while the freely expanding ejecta are presumably masked by the optically thick CSM, the radius of the blackbody that best fits the observations grows at $\approx 7000\,\mathrm{km\,s^{-1}}$. Such a velocity is characteristic of fast moving ejecta rather than optically thick CSM. This phase of radial expansion takes place before any spectroscopic signature of expanding ejecta appears in the spectrum and while both the spectroscopic data and the bolometric luminosity seem to indicate that the CSM is optically thick. We propose a geometrical solution to this puzzle, involving an aspherical structure of the CSM around PTF 12glz. By modelling radiative diffusion through a slab of CSM, we show that an aspherical geometry of the CSM can result in a growing effective radius. This simple model also allows us to recover the decreasing blackbody temperature of PTF 12glz. `SLAB-Diffusion`, the code we wrote to model the radiative diffusion of photons through a slab of CSM and evaluate the observed radius and temperature, is made available on-line.

Subject headings: keywords

1. INTRODUCTION

Type IIn supernovae (SNe) are characterized by prominent and narrow-to-intermediate width Balmer emission lines in their spectra (Schlegel 1990; Filippenko 1997; Smith 2014; Gal-Yam 2016). Rather than a signature of the explosion itself, this spectral specificity is presumably the result of the photoionization of a dense, Hydrogen-rich, circumstellar medium (CSM) which is ejected from the SN progenitor prior to the explosion.

The Type IIn class is not a well-defined category of objects, as many SNe show the characteristic narrow Balmer lines in their spectra, sometime during their evolution. These lines are the signature of an external physical phenomenon highly dependent on the surrounding environment, rather than of any intrinsic property of the explosion. Depending on the spatial distribution and physical properties of the CSM, these lines may persist for days ("flash spectroscopy", Gal-Yam et al. 2014; Khazov et al. 2016; Yaron et al. 2017), weeks (e.g., SN 1998s, Li et al. 1998; Fassia et al. 2000, 2001; SN 2005gl, Gal-Yam et al. 2007; SN 2010mc, Ofek et al. 2013a), or years (e.g., SN 1988Z, Danziger & Kjaer 1991; Stathakis & Sadler 1991; Turatto et al. 1993; van Dyk et al. 1993; Chugai & Danziger 1994; Fabian & Terlevich 1996; Aretxaga et al. 1999; Williams et al. 2002; Schlegel & Petre 2006; Smith et al. 2017; 2010 jl, Patat et al. 2011; Stoll et al. 2011; Gall et al. 2014; Ofek et al. 2014c).

In the last decades, the physical picture governing SN IIn explosions and the wider family of "interacting" SNe - SNe whose radiation can be partially or completely accounted for by the ejecta crashing into a dense surrounding medium - has become clearer (see e.g., Chevalier 1982, Chugai & Danziger 1994, Chugai et al. 2004, Ofek et al. 2010, Chevalier & Irwin 2011, Ginzburg & Balberg 2014, Moriya & Maeda 2014). In recent years, there is growing evidence that, in the majority of cases, the high-density CSM originates from explosive phenomena taking place in the months to years prior to the SN

[1] Department of Particle Physics and Astrophysics, Weizmann Institute of Science, Rehovot 76100, Israel.
[2] Racah Institute of Physics, The Hebrew University, Jerusalem 91904, Israel.
[3] Desy Zeuthen, 15738 Zeuthen, Germany.
[4] California Institute of Technology, 1200 East California Boulevard, MC 278-17, Pasadena, CA 91125, USA.
[5] Physics Department, Technion Israel Institute of Technology, 32000 Haifa, Israel.
[6] Haifa Center for Theoretical Physics and Astrophysics, Faculty of Natural Sciences, University of Haifa, Haifa 3498838, Israel
[7] Department of Astronomy, The Oskar Klein Center, Stockholm University, AlbaNova, 10691 Stockholm, Sweden.
[8] Department of Astronomy, University of Maryland, College Park, MD 20742-2421, USA.
[9] Cahill Center for Astrophysics, California Institute of Technology, Pasadena, CA, 91125, USA.
[10] Spitzer Science Center, California Institute of Technology, Pasadena, CA 91125.
[11] Infrared Processing and Analysis Center, California Institute of Technology, Pasadena, CA 91125, U.S.A.
[12] School of Physics and Astronomy, Tel Aviv University, 69978 Tel Aviv, Israel.
[13] Lawrence Berkeley National Laboratory, Berkeley, CA, 94720, USA.
[14] Department of Astronomy, University of California, Berkeley, CA, 94720-3411, USA.

explosion. One piece of evidence supporting this conclusion is the direct detection of the so-called precursors (luminous outbursts) in the months to years prior to the SN explosion (e.g., Foley et al. 2007; Pastorello et al. 2007; Fraser et al. 2013; Ofek et al. 2013a, 2014b, 2016; Elias-Rosa et al. 2016; Thöne et al. 2017). Several theoretical mechanisms have been suggested to explain extreme mass-loss episodes in the final stages of stellar evolution (e.g., Woosley et al. 2007; Quataert & Shiode 2012; Chevalier 2012; Soker & Kashi 2016).

While in normal core-collapse SNe, the radiation-mediated shock breaks out upon reaching the stellar surface, producing a strong blast in the UV and X-rays (Nakar & Sari 2010; Rabinak & Waxman 2011), in the case of SNe IIn the ejecta may crash into the optically thick CSM. The radiation-dominated and radiation-mediated shock runs into the CSM surrounding the star and goes on propagating into it as long as $\tau \gtrapprox c/v_{sh}$, where τ is the optical depth from the shock to the edge of the wind, v_{sh} is the shock velocity, and c is the speed of light (e.g., Ofek et al. 2010). When $\tau \sim c/v_{sh}$, (this condition is verified when the timescale for photons to diffuse from the shocked region to the photosphere becomes comparable to the dynamical timescale of the shock), the shock breaks out: photons diffuse ahead of the shock faster than the ejecta and radiation can escape ahead of the shock (Weaver 1976). After the shock breakout, in the presence of massive CSM above the shock, the radiation-dominated shock transforms into a collisionless shock (Katz et al. 2011; Murase et al. 2011, 2014). The collisionless shock slows down the ejecta and converts its kinetic energy into hard X-ray photons (Katz et al. 2011; Murase et al. 2011, 2014). If the optical depth of the CSM above the shock is high enough, the X-rays generated in the collisionless shock are converted into UV and visible radiation (e.g., Chevalier & Irwin 2012; Svirski et al. 2012). Without a sufficient optical depth though, the bulk of the X-ray photons will not convert into optical photons.

As far as a spectral signature is concerned, the common picture explaining SNe IIn observations is as follows. As long as the CSM is optically thick, the photosphere which emits the continuum is located in the unshocked CSM, masking the observer's view of the shock. The radiation from the shock propagates upstream and photoionizes the slowly moving CSM, resulting in relatively narrow Balmer recombination emission lines in the SN spectrum. As the shock reaches the optically thin medium, broader components can appear in the spectrum - maybe arising from the shocked zone forming at the contact discontinuity between the decelerated ejecta and the shocked CSM (Chugai et al. 2004). Alternatively, if the CSM is optically thin, lines from the fast moving SN ejecta, generated in inner regions, may become visible (e.g., Chevalier & Fransson 1994).

Observing SNe IIn at wavelengths where the collisionless shock radiates most - namely UV and X-rays - has the potential to unveil precious information about the explosion mechanism and the CSM properties (e.g., Ofek et al. 2013b). In particular, it may provide a much better estimate of the bolometric luminosity of the event. In this paper, we present and analyse the UV and visible-light observations of PTF 12glz, a SN IIn observed in a joint campaign by *GALEX* and the Palomar Transient Factory (PTF) and detected in the UV. PTF 12glz is one of the six SNe discovered during this campaign (Ganot et al. 2016). The survey was carried out as a proof-of-concept for the *ULTRASAT* mission (Sagiv et al. 2014).

Observations of SNe IIn are usually analyzed within the framework of spherically symmetric models of CSM. However, resolved images of stars undergoing considerable mass loss (e.g., η Carinae; Davidson & Humphreys 1997, 2012), as well as polarimetry observations (Leonard et al. 2000; Hoffman et al. 2008; Wang & Wheeler 2008; Reilly et al. 2017) suggest that asphericity should be taken into account for more realistic modeling. Asphericity of the CSM has recently been invoked to interpret the spectrocopic and spectropolarimetric observations of the Type IIn SN SN 2012ab (Bilinski et al. 2017) and SN 2009ip (Mauerhan et al. 2014; Smith et al. 2014; Levesque et al. 2014; Reilly et al. 2017). In this paper, we show that the light curve of PTF 12glz may be interpreted as evidence for aspherical CSM.

We present the aforementioned observations of PTF 12glz in §2. In §3, we present the analysis of these observations and the puzzling inconsistency between the spectroscopic and photometric observations. In §4, we model the radiative diffusion of photons through an aspherical slab and propose a solution to this puzzle. We then summarize our main results in §5. In the Appendix, we make available `SLAB-Diffusion`(Soumagnac 2018, Codebase: `https://github.com/maayane/SLAB-Diffusion`), a computer code for modeling radiation through a slab of CSM.

2. OBSERVATIONS AND DATA REDUCTION

In this section, we present the observations of PTF 12glz by the *GALEX*/PTF UV wide-field transient survey. This campaign, conducted during a nine-week period from 2012 May 24 through 2012 July 28, used the *GALEX NUV* camera to cover a total area of about 600 deg^2 over 20 times with a three-day cadence, while PTF observed the same region with a two-day cadence (Ganot et al. 2016).

2.1. *Discovery*

PTF 12glz was discovered on 2012 July 7 by the PTF (Law et al. 2009; Rau et al. 2009) automatic pipeline reviewing potential transients in the data from the PTF camera mounted on the 1.2 m Samuel Oschin telescope (P48, Rahmer et al. 2008). The image processing pipeline is discussed in Laher et al. (2014) and the photometric calibration is described in Ofek et al. (2012). The SN is associated with an $r = 18.51$ mag galaxy, SDSS[15]J155452.95+033207.5, shown in Figure 1 and modelled in section 3.2. The coordinates of the object, measured in the PTF images are $\alpha = 15^h54^m53^s.04$, $\delta = +03^d32'07''.5$ (J2000.0). The redshift $z = 0.0799$ and the distance modulus $\mu = 37.77$ were obtained from the spectrum and the extinction was deduced from Schlafly & Finkbeiner (2011) and using the extinction curves of Cardelli et al. (1989). All these parameters are summarized in Table 1.

Previous PTF observations were obtained in the years prior to the SN explosion, but no previous detection of

[15] Sloan Digital Sky Survey; York et al. (2000)

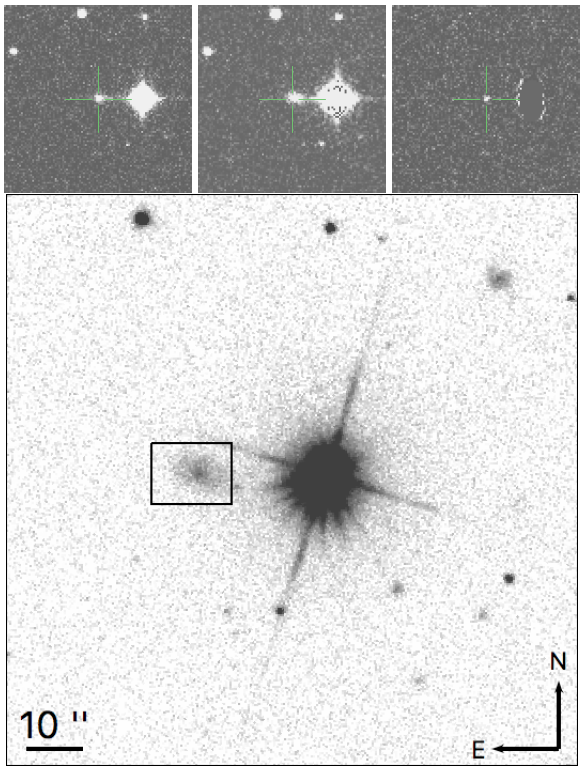


FIG. 1.— Top panels: (left to right) the discovery image, reference image, and subtracted P48 image of PTF 12glz. Lower panel: the SDSS image of J155452.95+033207.5, the host of the supernova PTF 12glz. The box encircles the host: $\alpha = 238.72100°$ and $\delta = 3.53542°$. Credit: SDSS.

TABLE 1

Parameter	Value
right ascension α ($J2000$)	238.721000 deg
declination δ ($J2000$)	3.535421 deg
redshift z	$z = 0.0799$
distance modulus μ	37.77 mag
galactic extinction E_{B-V}	0.13 mag

NOTE. — Summary of PTF 12glz observational parameters.

any precursor outbearst exist. The most recent non-detection was on 2012 June 25. We present a derivation of the explosion epoch in § 3.4.

2.2. *Photometry*

PTF 12glz was observed in multiple bands for almost three years after discovery. The SN was monitored during a rising phase ($t < 36$ days) and a decay phase ($t > 243$ days) but not around peak luminosity. All the host-subtracted light curves are shown in Figure 2. The photometry is reported in electronic Table 2 and is available via WISeREP[16].

GALEX observations of the PTF 12glz field started on 2012 May 26 and 15 observations were obtained with a cadence of ~ 3 days. The *GALEX NUV* camera was operating in scanning mode and observed strips of sky in a drift-scan mode with an effective average integration time of 80 s, to a *NUV* limiting magnitude of 20.6 mag [AB]. The *GALEX* data reduction was done using tools[17] by Ofek (2014).

TABLE 2

Epoch (days)	Counts (arb.)	Mag (magAB)	Instrument
11.24	0.75 ± 0.13	20.38 ± 0.28	*GALEX* nUV
9.71	362.30 ± 86.30	20.60 ± 0.26	P48/R
185.48	-	19.01 ± 0.06	P60/g'
185.48	-	18.85 ± 0.04	P60/r'
185.48	-	18.40 ± 0.05	P60/i'

NOTE. — **Photometry.** This table is available in its entirety in machine-readable format in the online journal. A portion is shown here for guidance regarding its form and content. Time is shown relative to the estimated epoch at which the extrapolated light curve (based on Equation 1) is crossing zero: $t_0 = 2456097.58$ (2012 June 19), as derived in § 3.4. To compute the apparent magnitudes from the counts, the zero-point for the nUV data is $ZP_{nUV} = 20.08$ and the zero-point for the P48 data is $ZP_{P48} = 27.00$.

The P48 telescope was used with a 12K×12K CCD mosaic camera (Rahmer et al. 2008) and a Mould *R*-band filter. Data were obtained with a cadence of ~ 2 days, to a limiting magnitude of R ≈ 21 mag [AB]. For the data reduction of the P48 data, we used a pipeline developed by Mark Sullivan (Sullivan et al. 2006; Firth et al. 2015).

The robotic 1.52 m telescope at Palomar (P60; Cenko et al. 2006) was used with a 2048×2048-pixel CCD camera and g', r', i' SDSS filters. Data reduction of the P60 data was performed using the FPipe pipeline (Fremling et al. 2016). We calibrated the P60 data in the following way. The *r*-band light curve was scaled so that its average value during the time window covered by both telescopes matches the average value of the P48 *R*-band photometric data. The *g*-band and *i*-band data were scaled to match the synthetic photometry of the calibrated spectroscopic data (§ 2.3). The synthetic photometry used for the calibration and for other purposes in this paper was computed with the PyPhot[18] pipeline (Fouesneau, in preparation).

Although the photometric data available for PTF 12glz do not cover the peak, the data during the rise and decay allow to place an upper limit on the absolute magnitude at peak: with $M_r \lesssim -20$, PTF 12glz is at the bright-end of the observed SNe IIn, together with e.g., SN 2006gy (Ofek et al. 2007; Smith & McCray 2007), SNe 2008fq (Thrasher et al. 2008; Taddia et al. 2013) or SN 2003ma (Rest 2009; Rest et al. 2011). In particular, it is brighter than all SNe in the sample by Kiewe et al. (2012), which was designed to be unbiased.

2.3. *Spectroscopy*

Four optical spectra of PTF 12glz were obtained using the telescopes and spectrographs listed in Table 3. The two first spectra were taken during the light curve rise, and the two last ones during the decay, at the dates shown in Table 3. The spectra were used to determine the redshift $z = 0.0799$ from the narrow host lines (Hα and [OIII]). All the observations were cor-

[16] https://wiserep.weizmann.ac.il

[17] MATLAB Astronomy & Astrophysics Toolbox, https://webhome.weizmann.ac.il/home/eofek/matlab/

[18] http://mfouesneau.github.io/docs/pyphot/

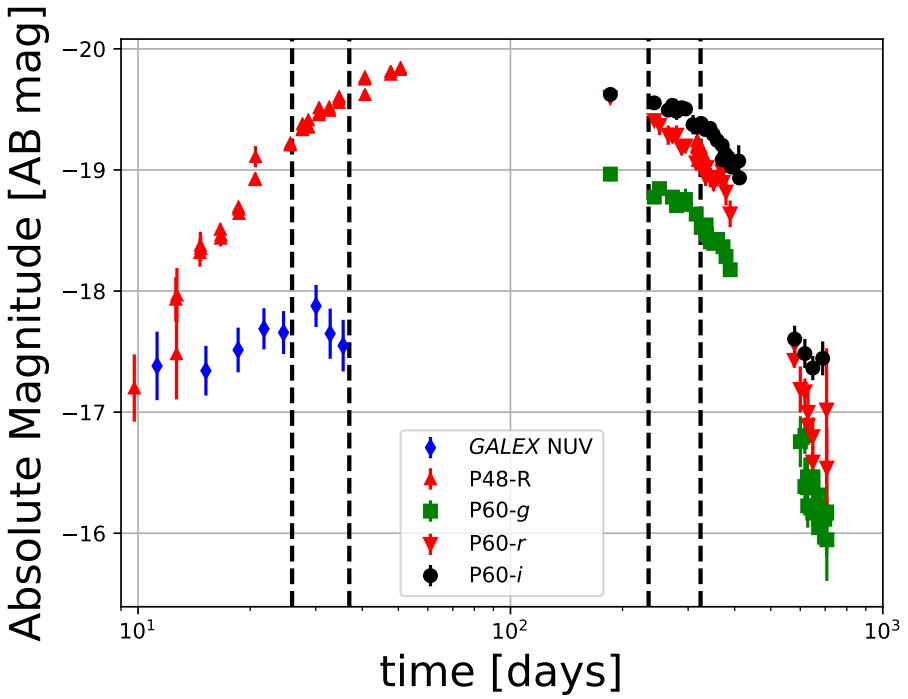


FIG. 2.— The light curve of PTF 12glz. Time is shown relative to the estimated epoch at which the extrapolated light curve (Equation 1) is crossing zero: $t_0 = 2456097.58$ (2012 June 19), as derived in § 3.4. Black dashed lines indicate dates at which spectroscopic data exist.

rected for a galactic extinction of $E_{B-V} = 0.13$ mag, deduced from Schlafly & Finkbeiner (2011) and using Cardelli et al. (1989) extinction curves, with the parameter $R \equiv A(V)/E_{B-V}$ (i.e. the ratio of total to selective extinction at V) set to the value $R = 3.1$. In § 3.3, we show that our qualitative results are not affected when varying R, e.g. within the interval given in Fitzpatrick (1999).

The spectroscopic observations were calibrated in the following way: the first two and the last spectra, for which we have contemporaneous P48 R-band data, were scaled so that their synthetic photometry matches the P48 R-band value. The third spectrum was scaled in the same way using the overlapping P60 r-band data instead.

The first and last spectra are shown in Figure 3 (the first two spectra are very similar, as well as the last two spectra) and all spectra are available from the Weizmann Interactive Supernova data REPository[19] (WISeREP, Yaron & Gal-Yam 2012).

TABLE 3

Date	Phase	Facility	Reference
2012 July 15	+26.2 days	P200	Oke & Gunn (1982)
2012 July 26	+36.9 days	P200	-
2013 February 9	+235.1 days	LRIS	Oke et al. (1994)
2013 May 9	+324.0 days	LRIS	-

NOTE. — Spectroscopic observations of PTF 12glz. The phase is given from the explosion epoch derived in § 3.4. The double-beam spectrometer (Oke & Gunn 1982) mounted on the 200 " Hale telescope at Palomar was used with a 1" slit, the 5500Å dichroic and the 316/7150 grating positionned at a grating angle of 24 deg 38.2 min. The Low-Resolution Imaging Spectrometer (LRIS) (Oke et al. 1994) spectrometer mounted on the 10 m Keck I telescope was used with a 1" slit, the 5600Å dichroic and the 400/3400 grism on the blue side.

3. ANALYSIS

3.1. *Spectroscopy*

The two early spectra, obtained during the rise of the light curve, are characteristic of interacting SNe: a blue continuum with strong and narrow Balmer lines, as well as weak He I (5876Å, 7065Å) narrow lines. At short wavelengths, the spectra show absorption from iron, as seen, for example, in SN 2010jl[20].

We fitted a blackbody spectrum to the six-point spectral energy distribution (corrected for redshift and extinction) obtained by combining (1) the observed photometry in the NUV and P48 R-band (2) the synthetic photometry of the spectra in the g, i and r SDSS bands. The best-fit temperatures and radii are shown in Table 4 and Figure 7 (as stars). In Figure 3, we show the synthetic and observed photometry derived for the earliest spectrum, on which is superimposed the calibrated spectrum and the best blackbody fit.

Both early spectra show strong and narrow Balmer lines, which for SNe IIn are interpreted as coming from the slow, unshocked, photoionized CSM. Their broad Lorentzian wings may be the signature of electron scattering, as the Hα photons diffuse ahead of the shock through the dense CSM (e.g., Chugai 2001). After subtracting the best-fit continuum from the spectra, we fitted the narrow Hα lines. We tried several linear combi-

[19] https://wiserep.weizmann.ac.il
[20] https://wiserep.weizmann.ac.il

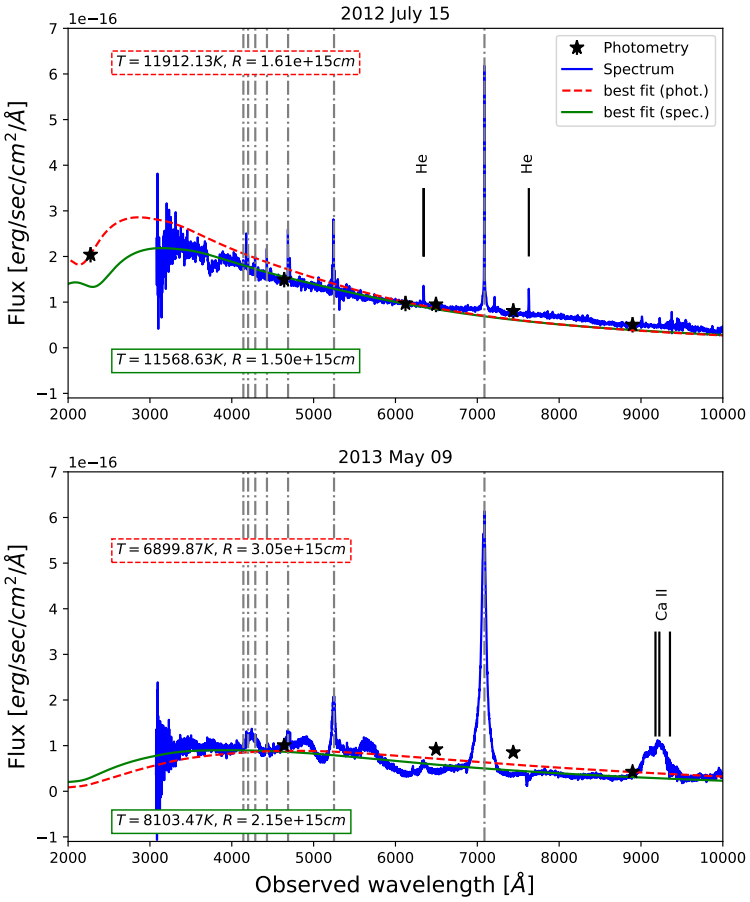


FIG. 3.— The earliest (top) and latest (bottom) observed spectra of PTF 12glz. Both spectra were calibrated to the R-band photometric measurement. Dashed lines indicate the redshifted emission lines for the Balmer series. Black stars show the combination of the observed (NUV and P48 R-band) and synthetic (g, r and i sdss bands) photometry. The dashed red line shows the blackbody curves that best fits the photometric data (and the best fit values are shown in the box with dashed contours), while the green continuous line shows the blackbody curve that bests fit to the spectroscopic data (and the best fit values are shown in the box with dashed contours). (A color version of this figure is available in the online journal).

nations of Gaussian and Lorentzian functions: the best fit is a superposition of a narrow Gaussian component with FWHM $\approx 100-200\,\mathrm{km\,s^{-1}}$ (i.e., unresolved), which we interpret as tracing the slow unshocked CSM and an intermediate Lorentzian component with FWHM $\approx 500-700\,\mathrm{km\,s^{-1}}$ (if some of the line-broadening comes from electron scattering, this is an upper limit of the CSM speed). The derived speeds and offsets are shown in Table 4. Figure 5 shows the line and the best fit for the latest spectrum.

No signature of expanding material is visible in the spectrum at this stage, which is consistent with a thick CSM obstructing the view of the SN ejecta at early times. We will show in § 3.3 how the photometric data are inconsistent with this picture.

The fits mentioned above, as well as all those mentioned in the rest of this paper, were performed using the `emcee` algorithm (Foreman-Mackey et al. 2013) to sample from the posterior probability distribution. We then used the ten combinations with the lowest χ^2 from the Monte Carlo Markov chain as initial conditions for an optimization algorithm to compute the best fit value (the maximum *a posteriori* value or "m.a.p.", in the terminology of Hogg et al. 2010). Note that we used MCMC to compute the posterior distribution and deduce the error bars on the one hand and on the other hand, used a distinct optimization algorithm to solve for the set of parameters maximizing the posterior, i.e. find the m.a.p. (which coincides with the maximum likelihood value and the minimum χ^2 value since the priors are uninformative). The reason we took this precaution - which turned out to be un-necessary - is that in the case of non-gaussian or non-symmetric marginalized posterior distribution, the m.a.p. may not fall necessary close to the median of the posterior distribution. In such cases, computing the position of the m.a.p. can be problematic and challenging, all the more when the χ^2 is noisy and full of local minima. The main challenge is then to choose an initial combi-

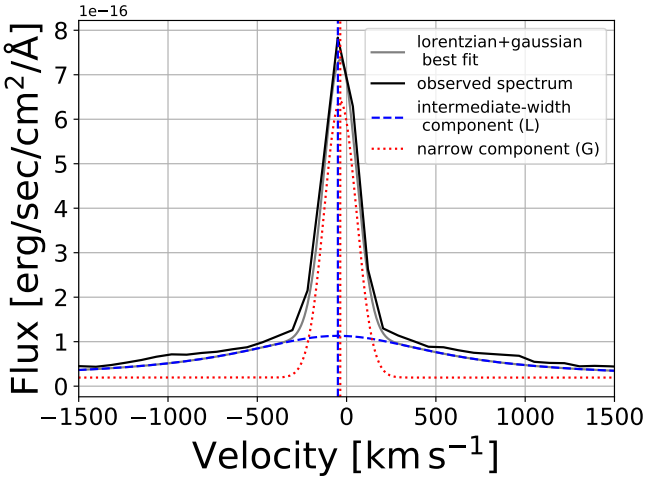


FIG. 4.— The Hα line profile on 2012 July 15 (earliest spectrum). The bold black line shows the observed spectrum. The red dotted line and blue dashed line are the narrow Gaussian (G) and intermediate-width Lorentzian (L) whose linear combination (in grey continuous line) best fits the data. The origin of the x-axis indicates the location of the Hα line at the host galaxy, at redshift $z = 0.0799$. The vertical lines indicate the center of each component: the narrow component is blueshifted by $\sim -30\,\mathrm{km\,s^{-1}}$ and the intermediate-width component is blueshifted by $\sim -50\,\mathrm{km\,s^{-1}}$.

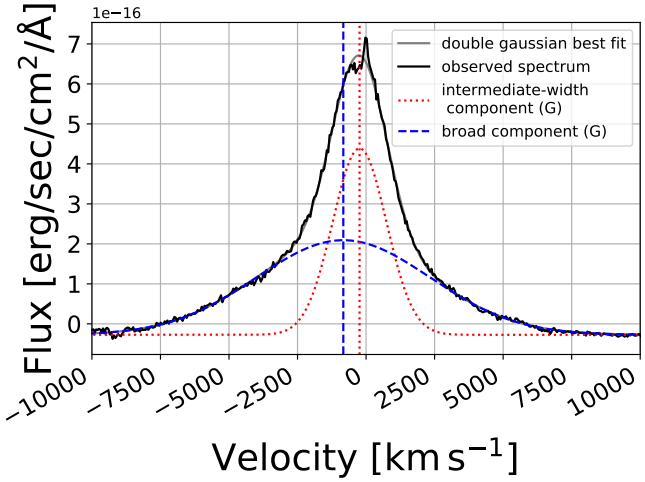


FIG. 5.— The Hα line profile on 2013 May 09 (latest spectrum). The bold black line shows the observed spectrum. The red dotted line and blue dashed line are the intermediate-width and broad Gaussian (G) components whose linear combination (in grey) best fits the data. The vertical lines indicate the center of each component: the narrow component is blueshifted by $\approx -230\,\mathrm{km\,s^{-1}}$ and the intermediate-width component is blueshifted by $\approx -830\,\mathrm{km\,s^{-1}}$.

nation of parameters values to give a minimization algorithm (most minimization algorithms, require to be given an initial combination of parameters from which to start their search for the minimum). The 10 sets of parameters from the chain giving the lowest χ^2 is a reasonable yet somewhat arbitrary choice of such initial condition. In the current case, since the posterior distribution is reasonably close to a Gaussian and well-behaved, the m.a.p. coincides with the median of the posterior distribution.

When errors are noted, they correspond to the 1σ limits of the marginalized posterior distributions.

The interpretation of the late-time spectra of Type IIn SNe should be made with the complexity caused by CSM interaction in mind. In "normal" type II SNe, the ejecta that become optically thin at late times are heated from the inside by two sources of energy: (1) remaining thermal deposition from the original heat of the explosion and (2) radioactivity. The late, or "nebular" spectrum shows no clear continuum, and its emission lines reflect the expansion of the ejecta in which they formed. In SNe IIn, the CSM interaction may continue to dominate the spectrum at late times, e.g., because the ejecta is heated by the shock wave propagating backward from the CSM into its outermost layers (Chevalier & Fransson 2003).

The two late-time spectra of PTF 12glz look similar (the latest spectrum is shown in Figure 3): they show a weak continuum in the red, a pseudo-continuum presumably formed by the superposition of narrow [Fe II] emission lines in the blue (e.g., Kiewe et al. 2012) and several broad emission lines. The temperatures and radii derived by fitting a blackbody curve to the observed spectrum are listed in Table 4 and compared to the parameters derived from photometry in Figure 7. Both spectra show broad Balmer emission lines. The derived speeds and redshifts are presented in Table 4 and Figure 5 shows the line and the best fit for the latest spectrum. The Hα lines are best fit by a linear combination of an intermediate-width Gaussian component with $FWHM \approx 2000\,\mathrm{km\,s^{-1}}$ that is offset to the blue by $\approx 250\,\mathrm{km\,s^{-1}}$ relative to the galaxy rest-frame and a broad Gaussian component with $FWHM \approx 8000\,\mathrm{km\,s^{-1}}$ that is offset to the blue by $\approx 1000\,\mathrm{km\,s^{-1}}$ relative to the galaxy rest frame. The intermediate-width component could come from the shocked gas in a cold dense shell forming at the contact discontinuity between the decelerated ejecta and the shocked CSM, which is reheated by X-rays and UV radiation from the shock. The broad component velocities are too high to originate from the CSM: they are rather characteristic ejecta velocity values. We deduce from these velocities that the ejecta has - at least partially - emerged through the optically thick layers of the CSM.

Both late spectra also show emission from the Ca II IR triplet. This is commonly seen in late time-interacting SNe, e.g., in the type IIn SN 2005ip (Boles et al. 2005; Stritzinger et al. 2012), the type Ic SN 2007dio (Kuncarayakti et al. 2018) and the type Ia-csm PTF 11kx (Dilday et al. 2012; Silverman et al. 2013; Graham et al. 2017), as well as in other types of SNe.

3.2. *Host galaxy*

We retrieved science-ready imaging data from the several surveys, summarized in Table 5: the Galaxy Evolution Explorer (*GALEX*) general release 7 (GR7) (Martin et al. 2005), the Panoramic Survey Telescope and Rapid Response System (Pan-STARRS; PS1) data release 1 (DR1) (Flewelling et al. 2016) and the Sloan Digital sky survey data release 9 (DR9) (SDSS; Ahn et al. 2012). We used the software package `LAMBDAR` (Lambda Adaptive Multi-Band Deblending Algorithm in R; Wright et al. 2016) that is based on Bourne et al. (2012) to perform multi-band matched aperture photometry (i.e., taking into account different pixel scales and point-spread functions). The absolute flux calibration was done against instrument-specific zero points (For details on the pho-

TABLE 4

Date	Continuum		Hα narrow comp.		Hα intermediate comp.		Hα broad comp.	
	T_{BB} [K]	R_{BB} [10^{15}cm]	Δv [km s^{-1}]	$FWHM$ [km s^{-1}]	Δv [km s^{-1}]	$FWHM$ [km s^{-1}]	Δv [km s^{-1}]	$FWHM$ [km s^{-1}]
2012 July 15	11570^{+350}_{-400}	$1.50^{+0.11}_{-0.07}$	−35	110	−50	680	-	-
2012 July 26	8400^{+2780}_{-440}	$2.91^{+0.36}_{-0.92}$	−80	240	−100	530	-	-
2013 February 09	8200^{+340}_{-350}	$2.56^{+0.24}_{-0.20}$	-	-	−270	1990	−1070	8580
2013 May 09	8100^{+420}_{-390}	$2.15^{+0.26}_{-0.22}$	-	-	−240	2310	−830	7470

NOTE. — The table shows the best fit values of the continuum and Hα lines in the four spectra of PTF 12glz. The early spectra are best fit with a linear combination of a narrow Gaussian component (left column) and an intermediate-width Lorentzian component (central column). The late spectra are best fit with a linear combination of an intermediate-width Gaussian component (central column) and a broad Gaussian component (right column). Δz is the shift of the centre of each component compared to the galaxy rest frame (the negative values mean that the component is blueshifted).

TABLE 5

Instrument	Filter	Wavelength (Å)	Brightness ($\mathrm{mag_{AB}}$)
GALEX	FUV	1542.3	21.55 ± 0.46
GALEX	NUV	2274.4	21.23 ± 0.51
SDSS	u'	3594.9	19.88 ± 0.17
SDSS	g'	4640.4	18.59 ± 0.07
SDSS	r'	6122.3	17.96 ± 0.08
PS1	i'	7439.5	17.75 ± 0.07
SDSS	z'	8961.5	17.59 ± 0.10
PS1	Y	9603.1	17.23 ± 0.19

NOTE. — **Photometry of the host galaxy.** The photometry is not corrected for Galactic reddening. The effective wavelengths were taken from the Spanish Virtual Observatory[a].

[a]https://svo.cab.inta-csic.es/

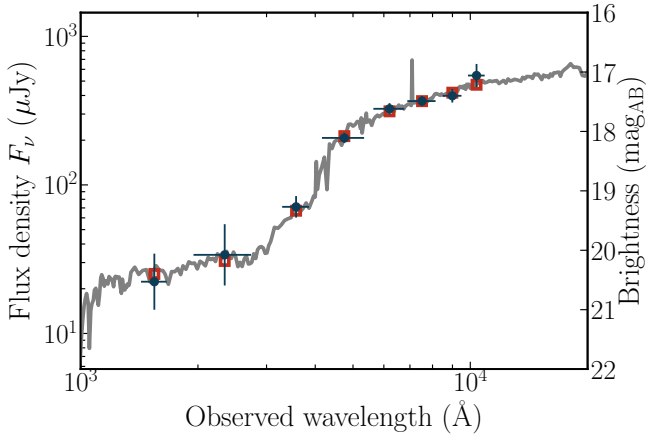


FIG. 6.— Spectral energy distributions of the host of PTF12glz from 1000 to 14000 Å. The observed magnitudes are displayed by the circles. The solid line displays the best-fit model of the SED with `Le Phare`. The squares are the model predicted magnitudes.

tometry see Schulze et al. in prep.).

We modelled the spectral energy distribution (SED) of the host galaxy with the software packages `Le Phare` on the web portal `GAZPAR`[21] (GAlaxy photometric redshifts (Z) & physical PARameters). We modelled the data using a grid of templates based on Bruzual & Charlot (2003) stellar population-synthesis models with the Chabrier initial-mass-function (Chabrier 2003), a star-formation history that is approximated by a declining exponential function, and a Calzetti et al. (2000) dust attenuation curve.

Figure 6 shows the measured galaxy photometry and the best fit. The SED can be adequately described by a template with a stellar mass of $\log M/M_\odot = 9.0^{+0.7}_{-0.2}$, a star-formation rate of $1.9^{+4.1}_{-0.7}$ $M_\odot\,\mathrm{yr}^{-1}$ and negligible attenuation [$E\,(B-V)=0$] (χ^2/number of filters = 1.3/8). Using the parametrisation of the mass-metallicity relation by Andrews & Martini (2013), we estimate the galaxy metallicity to be ~ 0.4–0.5 solar.

3.3. *The peculiar evolution of the blackbody radius*

Taking advantage of the multiple-band photometry coverage, we derived the temperature and radius of the blackbody that best fits the photometric data at each epoch (after correcting for redshift and extinction, interpolating the various data sets to obtain data coverage of coinciding epochs, and deriving the errors at the interpolated points with Monte Carlo Markov chain (MCMC) simulations). The derived best-fit temperatures T_{BB} and radii r_{BB} are shown in Figure 7. For the temperature MCMC fit, we adopted a broad, uninformative (flat) prior $T \in [5000, 25000]$. The edge values of the prior were chosen to contain the range of temperature observed e.g., in the SNe IIn sample by Taddia et al. (2013). The best fit temperatures T_{BB} should be seen as a lower limit on the temperature, since the spectra of SNe typically show a deficit of flux due to line-blanketing by metal lines.

In most epochs, this method implies fitting a blackbody spectrum to a two-point spectral energy distribution. Comparison with results derived from more constraining data detailed in § 3.1 - either spectroscopy (shown in red) or a combination of observed and synthetic photometry (shown in green) - suggests that this method leads to a slight overestimation of the radius and underestimation of the temperature.

The temperature T_{BB} drops from $\approx$ 15000 K to $\approx$ 8000 K during the rise and is stable at $\approx$ 6000 K during the decay phase. The decrease of T_{BB} at early time is well fitted by a power law t^n with index $n = -0.6$ and is consistent with the temperature evolution observed in

[21] https://gazpar.lam.fr

the sample by Taddia et al. (2013). However, PTF 12glz is relatively hot compared to the SNe IIn of this sample, where temperatures span between 11500 K and 5500 K, and compared to other well studied SNe IIn (e.g., 2006gy, Ofek et al. 2007; Smith & McCray 2007; SN 2005ip, Smith et al. 2009; SN 2010jl, Ofek et al. 2014c).

The derived radius grows by an order of magnitude, from $r_{BB} \approx 6 \times 10^{14}$ cm to $r_{BB} \approx 3 \times 10^{15}$ cm during the rising phase and is $\approx 4 \times 10^{15}$ cm during the light curve decay phase. Such a rise is puzzling within a picture where the optically thick CSM is supposed to mask the shock and the expanding material. To our knowledge, the measured blackbody radius of all SNe IIn observed to date either stalls after a slight increase (e.g., 2005kj, 2006bo, 2008fq, 2006qq, Taddia et al. 2013; 2006tf, Smith et al. 2008), or stays relatively constant at early times (e.g., SN2010jl Ofek et al. 2014c), or even supposedly shrinks (e.g., SN2005ip; SN2006jd, Taddia et al. 2013). Whereas a constant radius is consistent with the continuum photosphere being located in the unshocked optically thick CSM, the possible presence of clumps in the CSM that may expose underlying layers, has been invoked by Smith et al. (2008) to interpret observations of a stalling or shrinking radius.

In our case, the velocity at which r_{BB} grows, reaches $\approx 7000\,\mathrm{km\,s^{-1}}$, a value too large to trace the unshocked layers of the CSM or even the reverse shock. One may naively think that if the CSM was optically thin, then the observed radius would grow. However, in this case, it would be hard to convert efficiently the hard X-ray produced by the colisionless shock into optical radiation. In § 5 we propose one possible geometrical solution to this puzzle.

To investigate the effect of variations in the extinction and mimic the impact of errors in E_{B-V} on this results, we re-ran the analysis for the two extreme values of the parameter $R \equiv A(V)/E_{B-V}$ mentioned in Fitzpatrick (1999): 2.2 and 5.8. We observed an offset in the radius and temperature but our qualitative result - a growth in the radius at a velocity $\gtrapprox 7000\,\mathrm{km\,s^{-1}}$ and a decrease in the temperature - is maintained.

3.4. *Bolometric light curve*

Based on the measurement of r_{BB} and T_{BB}, we were able to derive the luminosity $L_{BB} = 4\pi R^2 \sigma T^4$ of the blackbody fits, shown in Figure 8. Since PTF 12glz was not observed at peak luminosity, we can only derive a lower limit on the peak luminosity $L_{BB,peak} > 4 \times 10^{43}\,\mathrm{erg\,s^{-1}}$. This makes PTF 12glz more luminous than SN 2008fq - the brightest SN of the Taddia et al. (2013) sample - and brighter than all but one SNe of the sample by Ofek et al. (2014a). This suggests that PTF 12glz is at the bright end of the SNe IIn luminosity range.

We fitted the light curve during the rise time with a function of the form

$$L = L_{\max}\{1 - \exp\left[(t_0 - t)/t_c\right]\}\,, \qquad (1)$$

(where t_0 is the time of zero flux, $L_{\max}$ is the maximum bolometric luminosity, and t_c is the characteristic rise time of the bolometric light curve). This allowed us to estimate the epoch at which the extrapolated light curve is crossing zero, which is used throughout this paper as the reference time $t_0\,(\mathrm{MJD}) = 56097.58$.

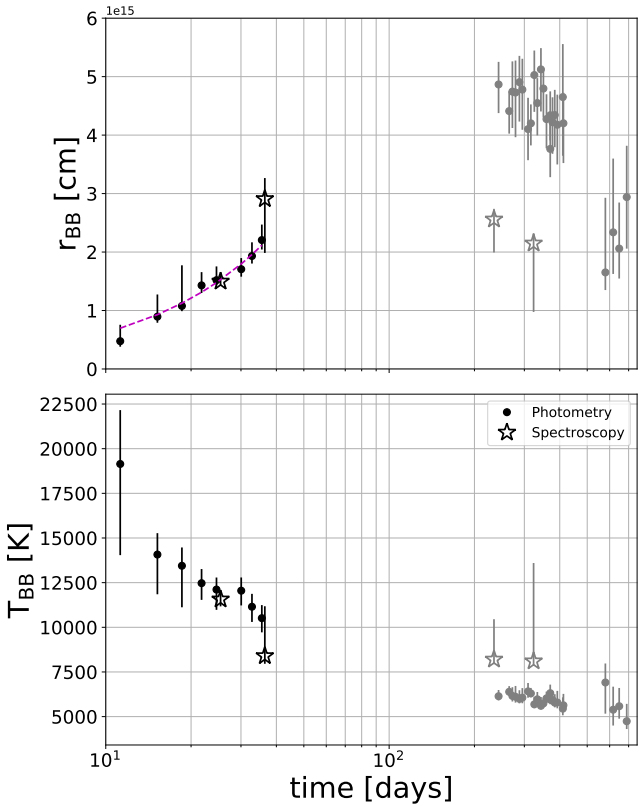


FIG. 7.— The evolution in time of: (1) the radius (top panel), (2) the temperature (lower panel) of a blackbody with the same radiation as PTF 12glz. The points were obtained by fitting a blackbody spectrum to the observed photometry, after interpolating the various data sets to obtain data coverage of coinciding epochs. The errors were obtained with MCMC simulations. The star symbols indicate the values derived by fitting a blackbody to the spectroscopic data. The dashed line in the top panel shows the best linear fit to the rising radius phase: a linear function with a slope of $\approx 7000\,\mathrm{km\,s^{-1}}$. At late times, the blackbody model for the spectral energy distribution may not be valid anymore (see, e.g., right panel in Figure 3): these points are shown in grey to emphasise that they are less reliable and should be taken cautiously.

As shown in Figure 8, L_{BB} decreases about twice as slowly as the 0.98 mag/100 d decline rate characteristic of the radioactive decay of ^{56}Ni to ^{56}Co and then to ^{56}Fe. If this decline was produced by the radioactive decay of ^{56}Ni, a Nickel mass of at least $14\,\mathrm{M_\odot}$ would be required to reach the bolometric luminosity of PTF 12glz (see Figure 8). The evolution of L should be taken cautiously, since at late time, a blackbody model for the spectral energy distribution may not be valid anymore, and so the temperatures and radii used to calculate L are less reliable.Although the late spectra analyzed in § 3.1 suggest that the ejecta may have emerged through the CSM at late times, the slow decline of L_{BB} hints at the fact that interaction may still play an important role in the radiation budget (this may happen through radiation from the reverse shock, or through processed radiation through the edge of the wind, or if the ejecta has only partially emerged through the CSM and is still interacting with it in some places).

3.5. *Mass of the CSM*

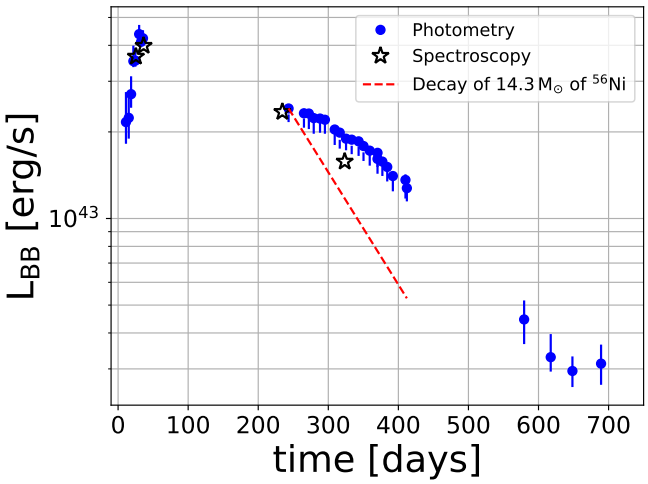


FIG. 8.— The evolution in time of the bolometric luminosity of a blackbody with the same radiation as PTF 12glz. The star symbols indicate the fits to the spectroscopic data. The dashed line shows the variation in luminosity caused by 14.3 $M_\odot$ of ^{56}Ni radioactively decaying to ^{56}Co and then to ^{56}Fe. L_{BB} decays ≈ 2 times slower, which suggests that radioactive decay is not sufficient to explain the decay of the light curve and that interaction or other sources of radiation play a role.

A very crude estimation of the swept-up CSM mass can be obtained by assuming that the ejecta mass is comparable to the mass of the CSM and that the bolometric luminosity L is accounted for by the conversion of the kinetic energy of the ejecta into radiation:

$$\int_t L(t)dt \lesssim \frac{1}{2} M_{\rm CSM} v_e^2 \ , \qquad (2)$$

where $M_{\rm CSM}$ is the mass of the CSM and v_e is the velocity of the ejecta. To an order of magnitude, this estimate will not be very different than estimates based on more realistic treatment of the hydrodynamics (e.g., Ofek et al. 2014c). We use the width $FWHM \approx 8000\,{\rm km\,s^{-1}}$ of the broad Hα component at late time (see section 3.1) as an approximation of the ejecta velocity v_e. From the measured bolometric luminosity shown in Figure 8, $\int_t L(t)dt \approx 10^{51}$ erg. Substituting this value in Equation 2 gives $M_{\rm CSM} \gtrsim 2 M_\odot$.

In interacting SNe, the optically thick CSM masks the explosion, which may leave an ambiguity about the underlying explosion type. In particular, type Ia SNe and core-collapse SNe exploding inside a thick CSM would result in similar observational signatures. The spectra would look similar at early time (as long as the explosion is masked by the CSM) and at very late times, when Ni has decayed and there is no more energy to illuminate the ejecta and create absorption lines in the spectrum. Here, the high value of the bolometric luminosity excludes the possibility that PTF 12glz is a masked SN Ia.

Another order of magnitude estimate of the mass can be obtained by assuming a wind density profile, $\rho_{\rm CSM}(r) = K\,r^{-2}$ and using the photon diffusion timescale (e.g., Ofek et al. 2010),

$$t_d \sim \frac{\kappa K}{c} \ , \qquad (3)$$

where κ is the CSM opacity. We assume $t_d \sim t_c$, where t_c is the characteristic rise time of the bolometric light curve. We estimate t_c by fitting the rising part of the bolometric light curve with the exponential function defined in Equation 1 and assuming $\kappa \approx 0.34\,{\rm cm^2\,g^{-1}}$. We obtain $t_c \sim 20$ day, and $K \approx 1.5 \times 10^{17}\,{\rm g\,cm^{-1}}$, which corresponds to high values of the density $\rho_{\rm CSM} \gtrsim 10^{-14}\,{\rm g\,cm^{-3}}$ (or a particle density of $n \sim 10^{10}\,{\rm cm^{-3}}$, assuming a mean number of nucleons per particle $\langle \mu_p \rangle = 0.6$) at the radii shown in Figure 7.

Measuring K allows us to estimate the mass of the CSM swept up by the ejecta, $M_{\rm CSM}(r) \sim 4\pi K r$ (assuming that the CSM extends on much higher scales than the stellar radius). Using the highest early-time radius r_{BB}, shown in Figure 7, as a lower limit of the maximum size of the shell of CSM surrounding the explosion, gives $M_{\rm CSM} \gtrsim 3\,M_\odot$, in good agreement with the estimates obtained with Equation 2.

For a wind density profile, $K = \dot{M}/(4\pi v_w)$, where v_w is the velocity of the CSM. Therefore, measuring K also gives us an estimation of the mass-loss rate. Using the width of the narrow Hα component during rise time, $FWHM \approx 200\,{\rm km\,s^{-1}}$, as a proxi of v_w (see Table 4), we obtain a large mass-loss rate $\dot{M} \sim 0.6\ M_\odot\ {\rm yr^{-1}}$, higher than the mass-loss rates observed in Taddia et al. (2013) and Kiewe et al. (2012) and comparable to the mass-loss rate of e.g., iPTF13z (Nyholm et al. 2017). Combining these estimates suggests that the CSM mass was ejected on a timescale of 1 to 10 years prior to the SN explosion.

We wish to emphasize that we made several simplifying assumptions in this section. In particular (1) we assumed a spherical symmetry of the CSM, (2) we assumed a wind profile of the CSM and (3) we assumed that the kinetic energy of the ejecta converts efficiently into radiation. Therefore, the numbers above have to be considered as order of magnitude estimates.

3.6. *Dust formation?*

At late times, the broad component of the Hα Balmer line is blueshifted by $\approx 1000\,{\rm km\,s^{-1}}$ relative to the galaxy rest frame. The intermediate component is also blueshifted, but by a velocity of $\approx 250\,{\rm km\,s^{-1}}$ which is consistent with a typical stellar velocity within the galaxy (see Table 4 and Figure 5). Several explanations have been proposed to explain the blueshift of emission line profiles in interacting SN. One possible explanation is the formation of dust which increasingly blocks the receding parts of the ejecta (e.g., as proposed in the case of the Type IIn SN 2010 jl, Smith et al. 2012; Gall et al. 2014). In our case, the blueshift of the broad component does not grow with time (see Table 4), meaning that if there is dust, it may have formed before the epoch of the first nebular spectrum. In our case, testing the wavelength dependency of the blueshift - a blueshift caused by dust would be stronger at bluer wavelengths - is tricky because the blended iron emission lines mask the structure of the $H\beta$ line profile. We tried to apply several filters on this area, to separate the possible broad Balmer components from Fe II blend structures, but the results remained inconclusive.

Other explanations have been proposed for the blueshift of emission lines. Fransson et al. (2014), for example, attributed the blueshift of emission lines to ra-

diative acceleration of the preshock gas by the SN radiation, whereas Smith et al. (2012) proposed a geometric explanation.

4. RADIATIVE DIFFUSION THROUGH A SLAB

The radiation from a SN exploding into a spherically symmetric CSM has been studied analytically, under simplifying assumptions (e.g., Chevalier 1982; Balberg & Loeb 2011; Ginzburg & Balberg 2014) and numerically (e.g., Falk & Arnett 1977; Moriya & Maeda 2014). The case of an aspherical CSM has been explored to a lesser extent (van Marle et al. 2010; McDowell et al. 2018). Exploring the expected effect of deviation from spherically symmetric CSM on the observables is all the more important since aspherical clouds of CSM around mass-ejecting stars seem to be common, e.g., in stars like η-Carinae (Davidson & Humphreys 1997) that have been proposed as SNe IIn progenitors (e.g., Gal-Yam et al. 2007; Gal-Yam & Leonard 2009). In this section, we attempt to determine whether a non-spherical geometry of the CSM around a SN can explain the growing radius and decreasing temperature observed in § 3.3. Solving for the exact shape of the CSM from a few observables in an ill-conditionned problem. Therefore, here our goal is merely to verify that a non-spherical geometry can explain the evolution of the observables. Given this goal, we consider a simple aspherical structure: a three-dimensional slab, infinite in two dimensions and perpendicular to the line of sight.

4.1. *Model and assumptions*

We have written a three dimensional computer program in python, `SLAB-Diffusion`, available on-line (Soumagnac 2018, Codebase: `https://github.com/maayane/SLAB-Diffusion`), in order to calculate the propagation of photons through a slab and simulate the main observables. The simple geometry we consider is illustrated in a cartoon in Figure 9. Following a similar approach as in Ginzburg & Balberg (2014), we replaced the hydrodynamical description of the SN explosion by a stationary model of the shock breakout. This is equivalent to neglecting the expansion of the gas due to the explosion and modelling the interaction between the shock and the CSM as an instantaneous deposition of energy in the slab.

The assumption of an instantaneous release of energy is justified when $t_d/t_e \gg 1$, where t_e is the timescale over which the energy of the ejecta is converted into radiation by deceleration, and t_d is the photon diffusion timescale (eq 3). The timescale t_e is given by

$$t_e = \frac{R_c}{v} \ , \tag{4}$$

where R_c is the radius at which the accumulated CSM mass is comparable to the ejecta mass and v is the ejecta velocity. Since $t_d/t_e = \tau v/c$, the condition $t_d/t_e \gg 1$ is satisfied, and the instantaneous energy deposition approximation is valid, as long as $\tau \gg c/v \sim 30$. This is indeed the case for the model parameters we infer for PTF 12glz: a wind velocity $v = 200\,\mathrm{km\,s^{-1}}$ (§ 3.1) with a mass-loss rate $\dot{M} \sim 0.6\,\mathrm{M_\odot\ yr^{-1}}$ (§ 3.5), yielding $R_c \sim 10^{15}\,\mathrm{cm}$ and $\tau \sim 200$.

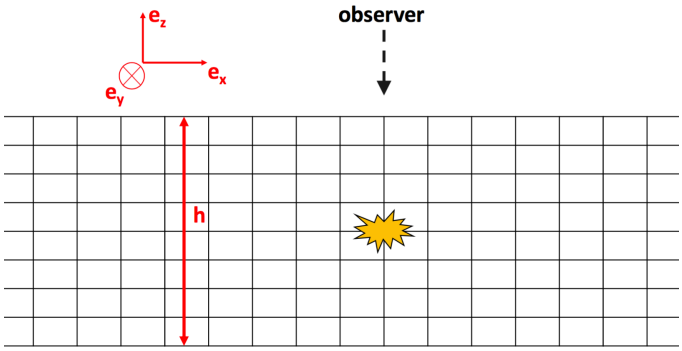


FIG. 9.— Sketch of the grid used to simulate radiative diffusion through a slab. The dimensions of the slab along the e_x and e_y coordinates are much larger than h, the dimension of the slab parallel to the line of sight. The initial energy of the explosion is deposited at $z = 0$, at a distance $h/2$ from the edge of the slab.

We assumed that the problem can be treated accurately within the diffusion approximation (i.e., assuming that $\tau \approx 1$ occurs close to the surface). Hence, the energy density u within the slab is described by the diffusion equation:

$$\frac{\partial u}{\partial t} = \nabla \cdot (D\vec{\nabla} u) \ , \tag{5}$$

where $D = c/(3\kappa\rho)$ is the diffusion coefficient. Here we explored three density profiles: a constant density profile, ρ, and two functions of the $\vec{e_z}$ coordinate: $\rho \propto |z|^{-1}$ and $\rho \propto z^{-2}$, where the origin of the z-axis is at the center of the slab. We leave the treatment of the angular dependency of D to further extensions of this work.

At the boundaries, the energy escapes from the slab and the flux $\vec{f}$ is linked to the density of energy through

$$||\vec{f}|| = \alpha c u \ , \tag{6}$$

where $\alpha \approx 1/4$ (the case $\alpha = 1/4$ corresponds to isotropic radiation). We discretized Equation 5 in a cartesian, three-dimensional grid (illustrated in a cartoon in Figure 9), using an explicit forward Euler scheme with $\Delta t D/(\Delta d)^2 < 0.1$ where Δd is defined for each coordinate and is the size of the mesh in each direction $\vec{e_x}$, $\vec{e_y}$ and $\vec{e_z}$. We assumed that D does not depend on the wavelength of the photons (i.e., we made the so called *grey* approximation). We solved a dimensionless version of Equation 5:

$$\frac{\partial u}{\partial t'} = \nabla \cdot (D'(z)\vec{\nabla} u) \ , \tag{7}$$

where $t' = tD(h)/h^2$ and $D'(z) = D(z)/D(h)$. In this case the boundary conditions are

$$||\vec{f}|| = \alpha v u \quad , \ v = c/v_d \ , \tag{8}$$

where $v_d = D(h)/h$. A slab with a width $h = 10^{16}\,\mathrm{cm}$, an opacity $\kappa = 0.34\,\mathrm{cm^2\,g^{-1}}$ and a constant mass density $\rho = 1 \times 10^{-16}\,\mathrm{g\,cm^{-3}}$ (corresponding e.g., to $3\,M_\odot$ of CSM in a slab with $L_x = L_y = 8\,h$), corresponds to

the unitless velocity $v \approx 1$ and a diffusion time $t_d = h^2 3\kappa\rho/c = 94$ days.

In order to minimize the effect of the finite size of the grid along $\vec{e_x}$ and $\vec{e_y}$, we took several precautions. We chose the dimensions of the grid along the $\vec{e_x}$ and $\vec{e_y}$ directions so that $L_x = L_y$ and $L_x \gg h$. We checked that L_x is large enough compared to h so that a change in L_x does not affect the results. Equation 8 only describes the boundary conditions along the $e_{\vec{z}}$ direction. We checked that we can apply reflective boundary conditions (i.e., $\vec{f} = \vec{0}$ at the boundaries) or absorbing boundary conditions (i.e., $u = 0$ at the boundary) along the $\vec{e_x}$ and $\vec{e_y}$ directions, without affecting the results. We also checked for convergence of the code with respect to the time steps.

4.2. *Results*

As photons diffuse in the slab, they reach the $z = h/2$ surface visible to the observer (see Figure 9). In Figure 10, we show the evolution of the total flux of energy escaping from the surface of a slab with $v = 1$, in response to an instantaneous deposition of energy at $t = 0$. We use the full-width at half maximum (FWHM) of the energy density u at the surface of the slab as a proxy for the radius seen by the observer (below we present another proxy for r_{BB}). In Figure 11, we show that the FWHM grows in time for all three checked density profiles $\rho = Const.$, $\rho \propto |z|^{-1}$ and $\rho \propto z^{-2}$. We checked that varying the parameter v does not change this qualitative result.

We would like to check whether our model can reproduce the decrease of the blackbody temperature T_{BB} observed in Figure 7, in addition to producing a growing radius. Here again, given the simplicity of our model geometry, we are interested in the evolution of T_{BB} rather than trying to fit its actual values. By modeling each cell of the $z = h/2$ surface as a blackbody with temperature $T \propto u(x, y)^{1/4}$ and summing up all the cell spectra, we can compute the overall spectrum of the surface. The resultant spectrum is well represented by a blackbody spectrum, which allows us to deduce the blackbody temperature of the surface. This strategy also provides an additional way to recover the growing radius, by using:

$$L = \int_S f \, ds = \sigma T_{BB}^4 4\pi r_{BB}^2 \, . \qquad (9)$$

In Figure 12, we show the evolution of the temperature T_{BB} and radius r_{BB}, assuming $h = 1 \times 10^{15}$ cm, a constant mass density $\rho = 3 \times 10^{-14}\,\mathrm{g\,cm^{-3}}$ and an input energy of 10^{51} erg. Using this energy (calculated in Equation 2) as the energy initially deposited in the slab, is equivalent to assuming that all the energy radiated by the SN explosion is released by the time it starts diffusing out through the CSM. This is only correct within the assumption that the characteristic timescale for diffusion is much larger than the characteristic timescale for interaction between the ejecta and the CSM, which we showed is a correct assumption in the case of PTF 12glz. Figure 12 shows that the aspherical geometry of the slab allows to recover the increase of the radius r_{BB} and the decrease of the temperature T_{BB} observed in Figure 7.

5. CONCLUSIONS

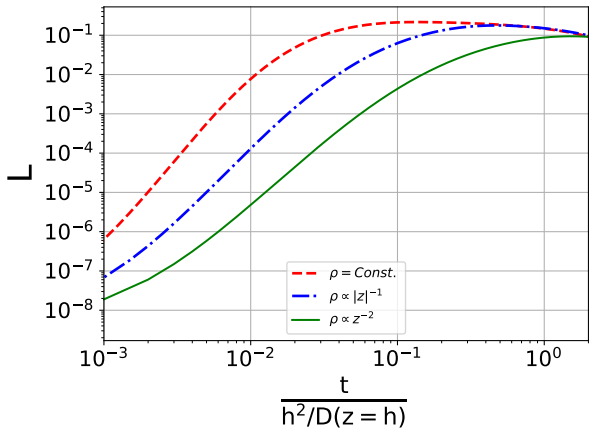


FIG. 10.— Luminosity $L = \int_S f \, ds$ released at the surface of a slab with $v = 1$, normalized so that the initial energy in the slab is 1. The luminosity is shown for a slab with a constant density profile (dashed line), a density profile $\rho \propto |z|^{-1}$ (dotted line) and a wind density profile $\rho \propto z^{-2}$ (continuous line).

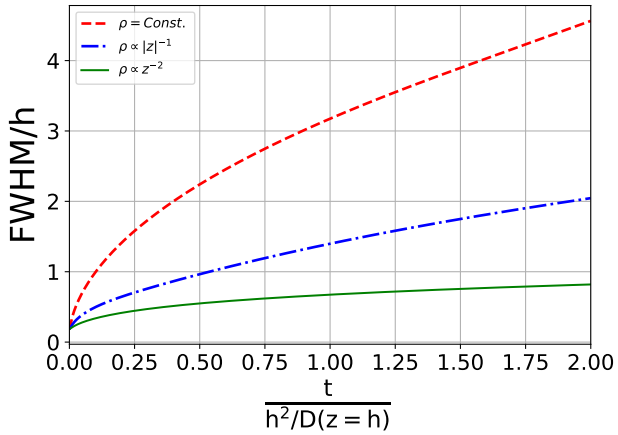


FIG. 11.— Full width at half-maximum (FWHM) of the density of energy u at the surface of a slab with $v = 1$. The FWHM is used as a proxy for the black body radius measured by the observer. The FWHM is shown for a slab with a constant density profile (dashed line), a density profile $\rho \propto |z|^{-1}$ (dotted line) and a wind density profile $\rho \propto z^{-2}$ (continuous line).

We presented the observations of the supernova PTF 12glz by the *GALEX* space telescope and ground-based PTF. Radioactive decay is not sufficient to explain the decay of the light curve of PTF 12glz and therefore other physical mechanisms must be involved. One possible - yet difficult to verify - scenario is that an internal engine powers the light curve. Another possible scenario - the standard explanation invoked in the case of Type IIn SNe, is that the light curve is powered by interaction between the ejecta and the CSM surrounding the SN.

In the case of PTF 12glz, the spectroscopic analysis is consistent with the following picture: at early times (two first spectra) both the ejecta and the shock are initially masked by a thick, slowly moving, photoionized CSM. At later times (two last spectra), the ejecta have emerged through - at least some of - the optically thick layers and have reached CSM layers that are optically thin enough to expose the ejecta. CSM interaction may still play a role at late times, e.g., by heating the ejecta from the

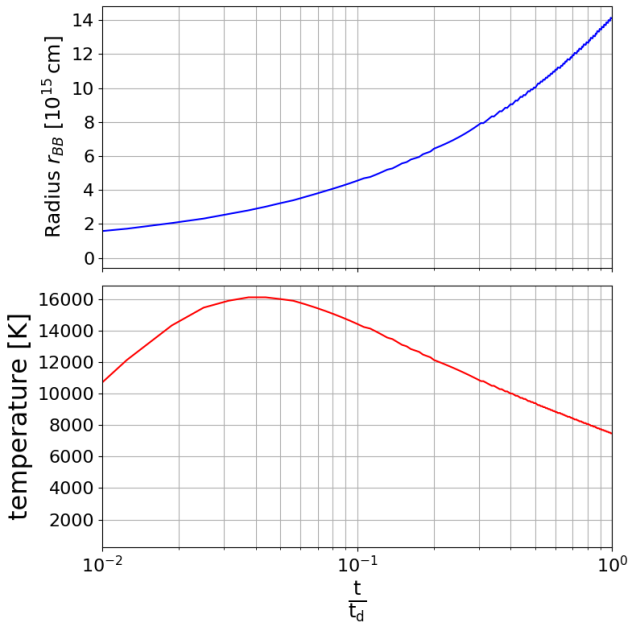


FIG. 12.— The evolution in time of: (1) the blackbody radius r_{BB} (top panel) and (2) the blackbody temperature (lower panel) at the surface of a slab with constant density. The diffusion equation was solved with an input energy $E_i = 10^{51}$ erg deposited in a slab of width $h = 10^{16}$ cm and constant mass density $\rho = 1 \times 10^{-16}\,\mathrm{g\,cm^{-3}}$, corresponding to $t_d = h^2 3\kappa\rho/c = 94$ days. The spectrum of the $z = h/2$ surface was deduced by summing the blackbody spectra of all the cells of the surface and T_{BB} was then deduced by fitting a blackbody to the resultant spectrum. The blackbody radius r_{BB} was deduced through the relation $r_{BB} = \sqrt{L/(4\pi\sigma T^4)}$. The aspherical geometry of the slab allows us to recover the increase of r_{BB} and the decrease in T_{BB}.

inside, and contributes to slowing the light curve decay.

The evolution of r_{BB} - the radius of the deepest transparent emitting layer - seems to contradict this picture. At early times, i.e., at the very time when the opaque CSM seemingly obstructs our view of any growing structure, r_{BB} grows by an order of magnitude, at a speed of $\sim 8000\,\mathrm{km\,s^{-1}}$. In addition to being inconsistent with the spectroscopic analysis, this is also in contradiction - to our knowledge - with all previous observations of either a constant or stalling blackbody radius in SNe IIn (as detailed in § 3.3).

If the bulk of the radiation from PTF 12glz does come from interaction, the explanation for the growing blackbody radius may be geometrical. The question then is whether any peculiar structure of the CSM around the progenitor can reproduce the observations. In this work, we considered a simple aspherical structure of CSM: a slab. We modeled the radiation from an explosion embedded in a slab of CSM by numerically solving the radiative diffusion equation in a slab with different density profiles: $\rho = Const.$, $\rho \propto |z|^{-1}$ and a wind density profile $\rho \propto z^{-2}$. Although this model is simplistic, it allows recovery of the peculiar growth of the blackbody radius r_{BB} observed in the case of PTF 12glz, as well as the decrease of its blackbody temperature T_{BB}. This configuration is not a unique geometrical solution and additional observations, e.g., of the polarization around PTF 12glz would have been necessary to make it less speculative.

As new wide-field transient surveys such as the Zwicky Transient Facility (e.g., Bellm et al. 2015; Laher 2018) are deployed, many more interacting SNe will be observed and quickly followed up with multiple-band observations. These may also be the brightest sources for the *ULTRASAT UV* satellite mission (Sagiv et al. 2014). Some of these interacting SNe may exhibit the same peculiarities as PTF 12glz. The methodology proposed in this paper offers a framework to analyze them. It could be elaborated upon, to model more complex aspherical geometries, e.g., η Carinae-like shapes of the CSM, and give more quantitative predictions of the observables.

M.T.S. thanks Jonathan Morag, Adam Rubin, Yi Yang, Doron Kushnir, Anders Nyholm and Chalsea Harris for useful discussions. M.T.S. acknowledges support by a grant from IMOS/ISA, the Ilan Ramon fellowship from the Israel Ministry of Science and Technology and the Benoziyo center for Astrophysics at the Weizmann Institute of Science.

E.O.O is grateful for the support by grants from the Israel Science Foundation, Minerva, Israeli Ministry of Science, the US-Israel Binational Science Foundation, the Weizmann Institute and the I-CORE Program of the Planning and Budgeting Committee and the Israel Science Foundation.

A.G.-Y. is supported by the EU via ERC grant No. 725161, the Quantum Universe I-Core program, the ISF, the BSF Transformative program, IMOS via ISA and by a Kimmel award.

This work is partly based on tools and data products produced by GAZPAR (https://gazpar.lam.fr) operated by CeSAM-LAM and IAP.

REFERENCES

Ahn, C. P., Alexandroff, R., Allende Prieto, C., et al. 2012, ApJS, 203, 21
Andrews, B. H., & Martini, P. 2013, ApJ, 765, 140
Aretxaga, I., Benetti, S., Terlevich, R. J., et al. 1999, MNRAS, 309, 343
Balberg, S., & Loeb, A. 2011, MNRAS, 414, 1715
Bellm, E. C., Kulkarni, S. R., & ZTF Collaboration. 2015, in American Astronomical Society Meeting Abstracts, Vol. 225, American Astronomical Society Meeting Abstracts #225, 328.04
Bilinski, C., Smith, N., Williams, G. G., et al. 2017, arXiv:1712.03370
Boles, T., Nakano, S., & Itagaki, K. 2005, Central Bureau Electronic Telegrams, 275

Bourne, N., Maddox, S. J., Dunne, L., et al. 2012, MNRAS, 421, 3027
Bruzual, G., & Charlot, S. 2003, MNRAS, 344, 1000
Calzetti, D., Armus, L., Bohlin, R. C., et al. 2000, ApJ, 533, 682
Cardelli, J. A., Clayton, G. C., & Mathis, J. S. 1989, ApJ, 345, 245
Cenko, S. B., Fox, D. B., Moon, D.-S., et al. 2006, PASP, 118, 1396
Chabrier, G. 2003, PASP, 115, 763
Chevalier, R. A. 1982, ApJ, 258, 790
—. 2012, ApJ, 752, L2
Chevalier, R. A., & Fransson, C. 1994, ApJ, 420, 268
Chevalier, R. A., & Fransson, C. 2003, in Lecture Notes in Physics, Berlin Springer Verlag, Vol. 598, Supernovae and Gamma-Ray Bursters, ed. K. Weiler, 171–194
Chevalier, R. A., & Irwin, C. M. 2011, The Astrophysical Journal Letters, 729, L6
Chevalier, R. A., & Irwin, C. M. 2012, ApJ, 747, L17
Chugai, N. N. 2001, MNRAS, 326, 1448
Chugai, N. N., & Danziger, I. J. 1994, MNRAS, 268, 173
Chugai, N. N., Blinnikov, S. I., Cumming, R. J., et al. 2004, MNRAS, 352, 1213
Danziger, I. J., & Kjaer, K., eds. 1991, European Southern Observatory Conference and Workshop Proceedings, Vol. 37, Supernova 1987A and other supernovae
Davidson, K., & Humphreys, R. M. 1997, ARA&A, 35, 1
Davidson, K., & Humphreys, R. M., eds. 2012, Astrophysics and Space Science Library, Vol. 384, Eta Carinae and the Supernova Impostors
Dilday, B., Howell, D. A., Cenko, S. B., et al. 2012, Science, 337, 942
Elias-Rosa, N., Pastorello, A., Benetti, S., et al. 2016, MNRAS, 463, 3894
Fabian, A. C., & Terlevich, R. 1996, MNRAS, 280, L5
Falk, S. W., & Arnett, W. D. 1977, ApJS, 33, 515
Fassia, A., Meikle, W. P. S., Vacca, W. D., et al. 2000, MNRAS, 318, 1093
Fassia, A., Meikle, W. P. S., Chugai, N., et al. 2001, MNRAS, 325, 907
Filippenko, A. V. 1997, ARA&A, 35, 309
Firth, R. E., Sullivan, M., Gal-Yam, A., et al. 2015, MNRAS, 446, 3895
Fitzpatrick, E. L. 1999, Publications of the Astronomical Society of the Pacific, 111, 63
Flewelling, H. A., Magnier, E. A., Chambers, K. C., et al. 2016, arXiv:1612.05243
Foley, R. J., Smith, N., Ganeshalingam, M., et al. 2007, ApJ, 657, L105
Foreman-Mackey, D., Hogg, D. W., Lang, D., & Goodman, J. 2013, Publications of the ASP, 125, 306
Fransson, C., Ergon, M., Challis, P. J., et al. 2014, ApJ, 797, 118
Fraser, M., Magee, M., Kotak, R., et al. 2013, ApJ, 779, L8
Fremling, C., Sollerman, J., Taddia, F., et al. 2016, A&A, 593, A68
Gal-Yam, A. 2016, ArXiv e-prints, arXiv:1611.09353
Gal-Yam, A., & Leonard, D. C. 2009, Nature, 458, 865
Gal-Yam, A., Leonard, D. C., Fox, D. B., et al. 2007, ApJ, 656, 372
Gal-Yam, A., Arcavi, I., Ofek, E. O., et al. 2014, Nature, 509, 471
Gall, C., Hjorth, J., Watson, D., et al. 2014, Nature, 511, 326
Ganot, N., Gal-Yam, A., Ofek, E. O., et al. 2016, ApJ, 820, 57
Ginzburg, S., & Balberg, S. 2014, ApJ, 780, 18
Graham, M. L., Harris, C. E., Fox, O. D., et al. 2017, ApJ, 843, 102
Hoffman, J. L., Leonard, D. C., Chornock, R., et al. 2008, ApJ, 688, 1186
Hogg, D. W., Bovy, J., & Lang, D. 2010, arXiv:1008.4686
Katz, B., Sapir, N., & Waxman, E. 2011, arXiv:1106.1898
Khazov, D., Yaron, O., Gal-Yam, A., et al. 2016, ApJ, 818, 3
Kiewe, M., Gal-Yam, A., Arcavi, I., et al. 2012, ApJ, 744, 10
Kuncarayakti, H., Maeda, K., Ashall, C. J., et al. 2018, ApJ, 854, L14
Laher, R. R. 2018, Robotic Telescope, 1, 329
Laher, R. R., Surace, J., Grillmair, C. J., et al. 2014, PASP, 126, 674
Law, N. M., Kulkarni, S. R., Dekany, R. G., et al. 2009, PASP, 121, 1395
Leonard, D. C., Filippenko, A. V., Barth, A. J., & Matheson, T. 2000, ApJ, 536, 239
Levesque, E. M., Stringfellow, G. S., Ginsburg, A. G., Bally, J., & Keeney, B. A. 2014, AJ, 147, 23
Li, W.-D., Li, C., Filippenko, A. V., & Moran, E. C. 1998, IAU Circ., 6829
Martin, D. C., Fanson, J., Schiminovich, D., et al. 2005, ApJ, 619, L1
Mauerhan, J., Williams, G. G., Smith, N., et al. 2014, MNRAS, 442, 1166
McDowell, A. T., Duffell, P. C., & Kasen, D. 2018, arXiv:1802.05152
Moriya, T. J., & Maeda, K. 2014, ApJ, 790, L16
Murase, K., Thompson, T. A., Lacki, B. C., & Beacom, J. F. 2011, Phys. Rev. D, 84, 043003
Murase, K., Thompson, T. A., & Ofek, E. O. 2014, MNRAS, 440, 2528
Nakar, E., & Sari, R. 2010, ApJ, 725, 904
Nyholm, A., Sollerman, J., Taddia, F., et al. 2017, A&A, 605, A6
Ofek, E. O. 2014, MATLAB package for astronomy and astrophysics, Astrophysics Source Code Library, ascl:1407.005
Ofek, E. O., Cameron, P. B., Kasliwal, M. M., et al. 2007, ApJ, 659, L13
Ofek, E. O., Rabinak, I., Neill, J. D., et al. 2010, The Astrophysical Journal, 724, 1396
Ofek, E. O., Laher, R., Law, N., et al. 2012, PASP, 124, 62
Ofek, E. O., Sullivan, M., Cenko, S. B., et al. 2013a, Nature, 494, 65
Ofek, E. O., Fox, D., Cenko, S. B., et al. 2013b, ApJ, 763, 42
Ofek, E. O., Arcavi, I., Tal, D., et al. 2014a, ApJ, 788, 154
Ofek, E. O., Sullivan, M., Shaviv, N. J., et al. 2014b, ApJ, 789, 104
Ofek, E. O., Zoglauer, A., Boggs, S. E., et al. 2014c, ApJ, 781, 42
Ofek, E. O., Cenko, S. B., Shaviv, N. J., et al. 2016, ApJ, 824, 6
Oke, J. B., & Gunn, J. E. 1982, PASP, 94, 586
Oke, J. B., Cohen, J. G., Carr, M., et al. 1994, in Proc. SPIE, Vol. 2198, Instrumentation in Astronomy VIII, ed. D. L. Crawford & E. R. Craine, 178–184
Pastorello, A., Smartt, S. J., Mattila, S., et al. 2007, Nature, 447, 829
Patat, F., Taubenberger, S., Benetti, S., Pastorello, A., & Harutyunyan, A. 2011, A&A, 527, L6
Quataert, E., & Shiode, J. 2012, MNRAS, 423, L92
Rabinak, I., & Waxman, E. 2011, ApJ, 728, 63
Rahmer, G., Smith, R., Velur, V., et al. 2008, in Proc. SPIE, Vol. 7014, Ground-based and Airborne Instrumentation for Astronomy II, 70144Y
Rau, A., Kulkarni, S. R., Law, N. M., et al. 2009, PASP, 121, 1334
Reilly, E., Maund, J. R., Baade, D., et al. 2017, MNRAS, 470, 1491
Rest, A. 2009, IAU Circ., 9092
Rest, A., Foley, R. J., Gezari, S., et al. 2011, ApJ, 729, 88
Sagiv, I., Gal-Yam, A., Ofek, E. O., et al. 2014, AJ, 147, 79
Schlafly, E. F., & Finkbeiner, D. P. 2011, ApJ, 737, 103
Schlegel, E. M. 1990, MNRAS, 244, 269
Schlegel, E. M., & Petre, R. 2006, ApJ, 646, 378
Silverman, J., Nugent, P. E., Gal-Yam, A., et al. 2013, in American Astronomical Society Meeting Abstracts, Vol. 221, American Astronomical Society Meeting Abstracts #221, 253.06
Smith, N. 2014, ARA&A, 52, 487
Smith, N., Chornock, R., Li, W., et al. 2008, ApJ, 686, 467
Smith, N., Mauerhan, J. C., & Prieto, J. L. 2014, MNRAS, 438, 1191
Smith, N., & McCray, R. 2007, ApJ, 671, L17
Smith, N., Silverman, J. M., Filippenko, A. V., et al. 2012, AJ, 143, 17
Smith, N., Silverman, J. M., Chornock, R., et al. 2009, ApJ, 695, 1334
Smith, N., Kilpatrick, C. D., Mauerhan, J. C., et al. 2017, MNRAS, 466, 3021
Soker, N., & Kashi, A. 2016, MNRAS, 462, 217
Soumagnac, M. T. 2018, SLAB-Diffusion: Modeling the radiative diffusion of photons through a slab of circumstellar material, doi:10.5281/zenodo.1488295
Stathakis, R. A., & Sadler, E. M. 1991, MNRAS, 250, 786
Stoll, R., Prieto, J. L., Stanek, K. Z., et al. 2011, ApJ, 730, 34
Stritzinger, M., Taddia, F., Fransson, C., et al. 2012, ApJ, 756, 173
Sullivan, M., Howell, D. A., Perrett, K., et al. 2006, AJ, 131, 960
Svirski, G., Nakar, E., & Sari, R. 2012, ApJ, 759, 108
Taddia, F., Stritzinger, M. D., Sollerman, J., et al. 2013, A&A, 555, A10
Thöne, C. C., de Ugarte Postigo, A., Leloudas, G., et al. 2017, A&A, 599, A129
Thrasher, P., Li, W., & Filippenko, A. V. 2008, Central Bureau Electronic Telegrams, 1507
Turatto, M., Cappellaro, E., Danziger, I. J., et al. 1993, MNRAS, 262, 128
van Dyk, S. D., Weiler, K. W., Sramek, R. A., & Panagia, N. 1993, ApJ, 419, L69
van Marle, A. J., Smith, N., Owocki, S. P., & van Veelen, B. 2010, MNRAS, 407, 2305
Wang, L., & Wheeler, J. C. 2008, ARA&A, 46, 433
Weaver, T. A. 1976, ApJS, 32, 233
Williams, C. L., Panagia, N., Van Dyk, S. D., et al. 2002, ApJ, 581, 396

Woosley, S. E., Blinnikov, S., & Heger, A. 2007, Nature, 450, 390
Wright, A. H., Robotham, A. S. G., Bourne, N., et al. 2016, MNRAS, 460, 765
Yaron, O., & Gal-Yam, A. 2012, PASP, 124, 668
Yaron, O., Perley, D. A., Gal-Yam, A., et al. 2017, Nature Physics, 13, 510
York, D. G., Adelman, J., Anderson, Jr., J. E., et al. 2000, AJ, 120, 1579